

## TOOLS AND RESOURCES

# ImaEdge – a platform for quantitative analysis of the spatiotemporal dynamics of cortical proteins during cell polarization

Zhen Zhang<sup>1,\*</sup>, Yen Wei Lim<sup>2,3,\*</sup>, Peng Zhao<sup>2,3</sup>, Pakorn Kanchanawong<sup>1,4,‡</sup> and Fumio Motegi<sup>1,2,3,‡</sup>

## ABSTRACT

Cell polarity involves the compartmentalization of the cell cortex. The establishment of cortical compartments arises from the spatial bias in the activity and concentration of cortical proteins. The mechanistic dissection of cell polarity requires the accurate detection of dynamic changes in cortical proteins, but the fluctuations of cell shape and the inhomogeneous distributions of cortical proteins greatly complicate the quantitative extraction of their global and local changes during cell polarization. To address these problems, we introduce an open-source software package, ImaEdge, which automates the segmentation of the cortex from time-lapse movies, and enables quantitative extraction of cortical protein intensities. We demonstrate that ImaEdge enables efficient and rigorous analysis of the dynamic evolution of cortical PAR proteins during *Caenorhabditis elegans* embryogenesis. It is also capable of accurate tracking of varying levels of transgene expression and discontinuous signals of the actomyosin cytoskeleton during multiple rounds of cell division. ImaEdge provides a unique resource for quantitative studies of cortical polarization, with the potential for application to many types of polarized cells.

This article has an associated First Person interview with the first authors of the paper.

**KEY WORDS:** Cortex, *C. elegans*, Zygote, Polarity, PAR protein, Actomyosin, Segmentation, Image processing

## INTRODUCTION

The cell cortex consists of a thin layer of cytoplasmic proteins and the actomyosin cytoskeleton organized beneath the plasma membrane (Salbreux et al., 2012). The cortex can be compartmentalized via the spatially biased dynamic behaviors of the actomyosin cytoskeleton and cortical proteins (Bray and White, 1988; Clark et al., 2014). These cortical proteins can diffuse laterally within the cortex and exchange between the cortex and the cytoplasm. The polarization of these cortical compartments, in turn, controls various aspects of metazoan development. For example, the establishment of apical and basolateral cortical domains in epithelial

cells allows for directional vesicle transport (Rodriguez-Boulán and Macara, 2014). Axons and dendrites also arise from asymmetrical segregation of cortical proteins in neuronal cells, allowing for the establishment of neural circuits (Knoblich, 2010).

The understanding of mechanisms underlying cortical polarization has long been a goal in the study of cell polarity. Robust quantitative analysis of protein dynamics at the cortex is integral towards this objective, but has remained technically challenging. While sophisticated imaging techniques have enabled cell and developmental biologists to attain higher-resolution images of cells, the dynamic process of cell polarization has not been sufficiently described. This is largely due to a lack of development of unbiased quantitative analyses of dynamic protein behaviors at the cortex (Myers, 2012). The spatiotemporal dynamics of cortical proteins are commonly represented either by a gallery of consecutive frames from time-lapse movies or by a kymograph with straight lines drawn at multiple locations of interest. Although they are simple to perform, these approaches are far from able to capture the full extent of information available in time-lapse movies. There are several computational tools that can track the position of cell edges and cortical proteins, but they are mostly optimized for cultured cells, which are typically labeled by overexpressed bright fluorescent probes with a largely uniform distribution (Tables S1 and S2) (Barry et al., 2015; Biro et al., 2013; Bosgraaf and Van Haastert, 2010; Dimopoulos et al., 2014; Dormann et al., 2002; Held et al., 2010; Hodneland et al., 2013; Machacek et al., 2009; Tsygankov et al., 2014; Wang et al., 2010). It has been a challenge to apply the existing tools to study cortical proteins in multicellular transgenic organisms such as developing embryos, mainly because of the weak fluorescence signals expressed in these systems, together with the complex and fluctuating cell contours. Additionally, although dedicated plasma membrane probes, such as GFP-tagged PH domain, can be used to aid in cortex segmentation (Balla and Varnai, 2009), the use of such probe takes up one valuable spectral channel, restricting the choice of fluorophores and constraining multi-color multi-protein analysis.

To overcome the aforementioned problems, we sought to develop a simple but robust method that can precisely locate the cell edge contours using the inhomogeneous distribution of fluorescence intensities of a polarity protein itself. This is an important prerequisite for investigating certain proteins that exhibit polarized distribution along the cortex, such as cortical polarity regulators and the actomyosin cytoskeleton (Goldstein and Macara, 2007; St Johnston and Ahringer, 2010). In the case of these proteins, segmentation using a single threshold value cannot capture the proper cell edges for the entire duration of cell polarization, during which the intensities and patterns of cortical

<sup>1</sup>Mechanobiology Institute, National University of Singapore 117411, Republic of Singapore. <sup>2</sup>Temasek Lifesciences Laboratory, Singapore 117604, Republic of Singapore. <sup>3</sup>Department of Biological Sciences, National University of Singapore, Singapore 117543, Republic of Singapore. <sup>4</sup>Department of Biomedical Engineering, National University of Singapore 117583, Republic of Singapore.

\*These authors contributed equally to this work

‡Authors for correspondence (biekp@nus.edu.sg; fmotegi@tll.org.sg)

© Z.Z., 0000-0001-6591-4522; Y.W.L., 0000-0002-8868-6435; P.Z., 0000-0001-7665-798X; P.K., 0000-0001-8765-3861; F.M., 0000-0001-9058-6559

proteins will change. These problems could be addressed in principle by using segmentation methods based on the progressive evolution of an active contour that is defined either by the minimization of a customized energy function or by parameter-free methods that track the local information from the cell edge (Ersoy et al., 2008a,b; Li et al., 2009; Nejati Javaremi et al., 2013; Song et al., 2017; Wu et al., 2015). These methods in practice involve relatively complex segmentation algorithms with multiple key input parameters, requiring significant user intervention to analyze large-scale datasets from long time-lapse movies, such as those obtained during cell polarization. Therefore, the important segmentation steps tend to be labor intensive, time consuming and error prone.

Here, we present a computational approach, implemented as a software called ImaEdge (IMaGE analysis of cell EDGE dynamics), which addresses the problems highlighted above. Instead of requiring a global threshold for defining the cortex, ImaEdge utilizes an adaptive gradient method to automatically determine the relevant parameters for all frames of a time-lapse movie, using the fluorescence intensity of the cortical protein of interest itself (Fig. 1). Firstly, the images are radially segmented using adaptive thresholds. The optimal cell contour is computed in accordance with the maximum average image intensity gradient without the creation of a complex energy function. Secondly, to detect the thickness of the cortical region, the cell contour is propagated inward until the maximum average intensity gradient is located. Thirdly, to obtain a global view of the dynamics and spatiotemporal evolution of cortical protein intensity, the cortex is sampled at specified intervals, and the temporal evolution is calculated by closest-sub-region linkage between adjacent frames. We demonstrate the capability of ImaEdge by quantifying the spatiotemporal dynamics of two cell polarity proteins, PAR-6 and PAR-2, and non-muscle myosin-II heavy

chain, NMY-2, during cell polarization in *Caenorhabditis elegans* embryos. ImaEdge was able to trace the local and global changes of cortical protein concentrations from one-cell to two-cell embryos without the need for dedicated cortical markers. ImaEdge is equipped with a graphical interface for ease of use by cell and developmental biologists [software user manual available on GitHub (<http://github.com/KanchanawongLab>)], thus providing a unique resource for a quantitative study of cortical polarization in various polarized cell types.

## RESULTS

### Monitoring cortical polarization in *C. elegans* zygotes

To develop a method to automatically determine the cell cortex region in every frame of a time-lapse movie, we used a classic example of cell polarization, the *C. elegans* zygote. The *C. elegans* zygote begins to polarize shortly after the entry of the sperm-donated centrosome (Cowan and Hyman, 2004, 2006; Hamill et al., 2002; O'Connell et al., 2000; Schumacher et al., 1998). Cortical actomyosin and partitioning defective (PAR) proteins become segregated into two distinct cortical domains along the anterior–posterior axis (Kemphues, 2000). The actomyosin network and the anterior PAR proteins (two PDZ-domain proteins PAR-3 and PAR-6, and atypical protein kinase C) initially localize throughout the cortex and then become segregated to the anterior cortex during polarization (Etemad-Moghadam et al., 1995; Hung and Kemphues, 1999; Tabuse et al., 1998). The posterior PAR proteins (PAR-1 kinase, PAR-2, and LGL-1) translocate from the cytoplasm onto the posterior cortex (Beatty et al., 2010; Boyd et al., 1996; Guo and Kemphues, 1995; Hoege et al., 2010). Extensive overlap between these two cortical domains is prevented by reciprocal inhibitory interactions between the anterior and the posterior PAR proteins (Cuenca et al., 2003; Hao et al., 2006; Hoege

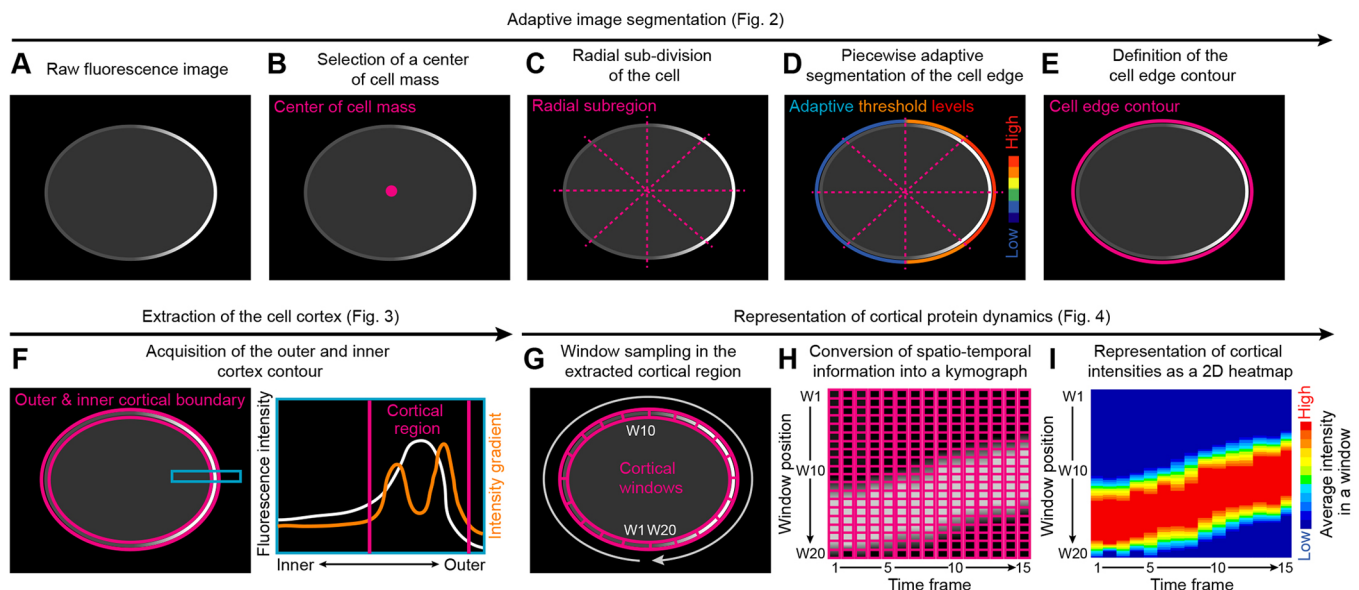


**Fig. 1. Analytical time line on the extraction of dynamic behavior of cortical proteins by ImaEdge.** ImaEdge adopts an adaptive gradient method to automatically determine the relevant parameters of cortical fluorescence intensity for all frames in a time-lapse movie. (A–E) The cell edge contour is defined by segmentation using adaptive thresholds in each sector region (see also Fig. 2). (A,B) The center of cell mass of the cell of interest is calculated from the first frame of the time-lapse movie. (C) This center of cell mass is used to radially sub-divide the cell of interest into subregions. (D) A binary threshold between the cell and the background is calculated for each sector region. (E) The cell contour is defined by connecting each sector. (F) Extraction of the cell cortex (see also Fig. 3). The cortical region enclosed by inner and outer boundaries (left) is detected by checking the average of image gradients along each distance level near the cortex. The cortex width is then identified when the two largest averages of image gradients are fully covered (right). (G–I) Representation of cortical protein dynamics (see also Fig. 4). (G) Sampling windows are equally spaced along the entire cortex. (H) The spatio-temporal information of cortical proteins is represented in a 2D kymograph. (I) The intensity of cortical proteins can be represented by a heatmap.

et al., 2010; Motegi et al., 2011). Since PAR-6 and PAR-2 have commonly been used as proxies for the anterior and the posterior PAR protein complexes, respectively (Cuenca et al., 2003; Goehring et al., 2011), we monitored mCherry::PAR-6 and GFP::PAR-2 in live zygotes (Fig. S1 and Movie 1).

### Adaptive radial segmentation of cell edges

The non-uniform distribution of cortical PAR proteins poses a major challenge for the accurate and unbiased segmentation of the cell cortex (Fig. 2A–C). Therefore, ImaEdge was designed to automate these processes while providing intuitive visual guides to allow a biologist full control of the process. ImaEdge first enhances the intensity contrast of the loaded image (MATLAB command: *imadjust*) as an initial processing step before subsequent segmentation. We implemented an adaptive radial segmentation algorithm to determine the contour of the cell edge in each frame of the time-lapse movies (Fig. 2D–I). The image of the first frame (either single-channel, or merged multi-channel) was binarized

using Otsu's method (Otsu, 1979), keeping the largest 8-connected binary region as the initial binary mask for the cell of interest, while discarding smaller regions. This yields the initial mask that captures the majority of the cell region, albeit with irregular edges that do not generally conform to the actual cell edge contour. Next, to obtain the accurate cell contour, the center of mass of the cell of interest was calculated. This position was used to radially sub-divide the region of the cell of interest into multiple sectors (typically 10) (Fig. 2D). A small margin (typically 35 pixels or 9.3  $\mu\text{m}$ ) was added to each sector to include a small portion of the out-of-cell background regions for accurate estimates of the background intensity. For each sector, a binary threshold between the cell and the background was calculated using Otsu's method (Fig. 2E–G). This serves as the starting estimate for the cell contour within a given sector. Subsequently, the largest 8-connected objects in all sectors were then merged into the whole-cell binary mask. The merged mask was median-filtered (typically a 10 $\times$ 10 pixels median filter) to smoothen the cell contour, especially to eliminate

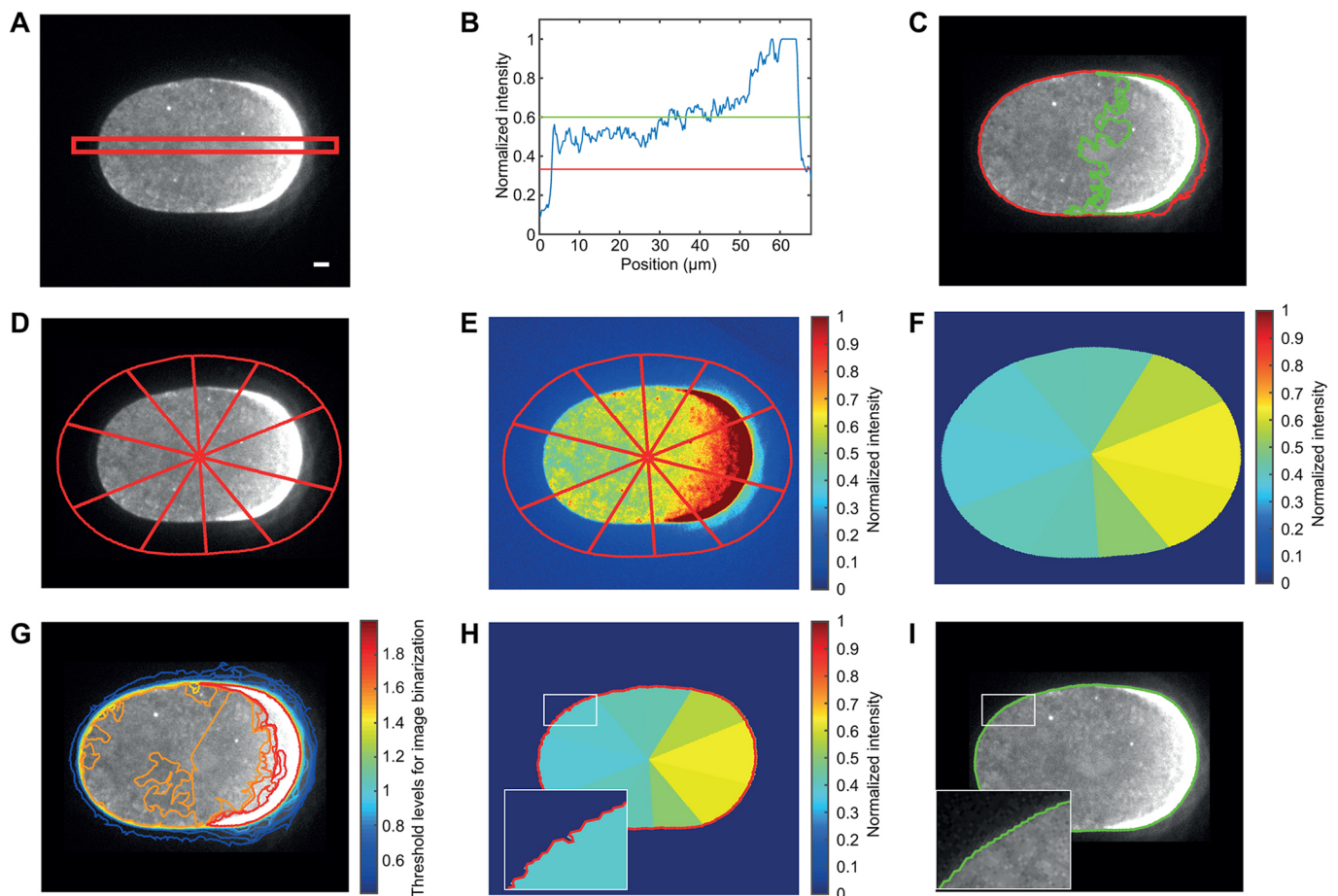


**Fig. 2. Automated adaptive radial segmentation of *C. elegans* zygotes expressing GFP::PAR-2.** (A) Fluorescence image of GFP::PAR-2 in a *C. elegans* zygote during prometaphase. GFP::PAR-2 is unevenly distributed along the cell cortex. Scale bar: 5  $\mu\text{m}$ . (B) Normalized intensity profile of GFP::PAR-2 along the anterior–posterior axis of the inset shown in a red rectangle in A. Green and red lines indicate the threshold levels corresponding to the contours shown in C. (C) Overlay of the GFP::PAR-2 image with two contours resulting from over-segmentation (green) and under-segmentation (red) by the single-threshold method. Green and red contours correspond to the green and red threshold levels respectively in B. (D,E) A cell of interest is radially divided into ten subregions for adaptive segmentation. GFP::PAR-2 is shown as a grayscale image (D) and as an intensity-heatmap (E). (F) Application of adaptive thresholds for each sub-region. The color in each sub-region shows the threshold level for segmentation of the cell edge contour. (G) Overlay of the GFP::PAR-2 image with the reconnected contours acquired by varying threshold levels relative to the Otsu's threshold in adaptive segmentation. (H) An overlay of the adaptive threshold levels in each sub-region with an unsmoothed cell contour (red). Each pixel within the cell is represented using its threshold. A magnified view of the white-boxed region is shown on the bottom left. (I) Overlay of the GFP::PAR-2 image with a smoothened cell contour (green). A magnified view of the white-boxed region is shown on the bottom left. Color bars in E,F,H show each protein intensity normalized to its maximum in E.

disjointed edges at the boundaries between sectors (Fig. 2H,I). The size of the median filter determines the extent to which the cell contour will be smoothened. For example, a larger median filter focuses more on the global cell morphology, while a smaller one better preserves local context along the cell edge. To find the optimal binary thresholds for these sectors, varying scaling factors within a customized range (typically from 50% to 120% in 2% increments) were applied to the initial Otsu threshold. To segment the cortical region, the intensity gradient map was calculated by applying a Sobel–Feldman filter to the contrast-enhanced image. The averaged image gradient with a specific contour was then calculated.

The optimal scaling factor was determined as the value which yields the maximum average image gradient. This was then multiplied with the Otsu threshold to generate the optimal threshold levels for all sectors. The same procedure is then applied to each time-lapse frame, thereby automatically segmenting the cell contour for the entire movie.

### Quantification of cortical protein spatiotemporal dynamics

Once the cell edge contours were defined, the thickness of the cortex was determined by computing a distance map relative to the segmented cell edge (Fig. 3 and Fig. 4A,E). The distance levels were propagated inward, allowing the calculation of the average image gradient for each distance level (Fig. 3B,C). The minimum distance that fully covers the first and second maximum spatial derivatives of the image gradient was then selected as the outer and inner boundaries of the cell cortex (Fig. 3D–G). Since cortical thickness may vary in different frames, this process was then iterated for all image frames, thereby automatically capturing the cortical width dynamics of the entire cell (Fig. 3H).

To quantify the spatiotemporal dynamics of fluorescence-tagged proteins at the cortex, the entire cortical region was subdivided into a user-defined number of sampling windows (typically 100). This

was done by placing uniformly spaced sampling points along the cell contour, which are then connected to their closest partner points along the inner boundary (Fig. 4A–H; Movie 2). The nearest box-oriented alignment was performed to align the leftmost sampled window to the closest window in every two consecutive frames. This was done by checking the Euclidean distance between the centers of two sampling boxes. The leftmost window was used as the starting point, and the other boxes were aligned consecutively in a clockwise fashion. ImaEdge continued searching for the closest window in the next frame and repeated the alignment until all windows were accurately assigned to all frames (Fig. 4D,H; Movies 2 and 3). The mean fluorescence intensity in each sampling window can then be calculated to represent the local intensity of proteins of interest at the cortex.

Recasting the spatiotemporal dynamics of the cortex into a rectilinear coordinate allows for direct comparison across multiple cells (Machacek et al., 2009). The spatiotemporal dynamics of cortical proteins can be represented in a 2D heat map, where positions of each sampling window are plotted against their respective frame numbers (Fig. 4I,J). For example, the entry value in the  $r^{\text{th}}$  row and  $c^{\text{th}}$  column of the 2D heat map is the mean intensity of the  $r^{\text{th}}$  sampling box in the  $c^{\text{th}}$  frame. To approximate the continuous form of the spatiotemporal dynamics of cortical proteins, the heat maps can also be smoothened with a 2D Gaussian filter with customizable standard deviations. The average intensity within a group of windows can also be calculated to represent the changes in the intensity of the cortical protein (Fig. 4K).

### Sensitivity to various signal-to-noise levels

Live imaging of long biological processes is often constrained by the fusion probe expression levels, the brightness and photostability of fluorophores, and the phototoxic susceptibility of the cells of interest. These factors often limit the achievable image quality. To determine the viable signal-to-noise level for robust quantitative

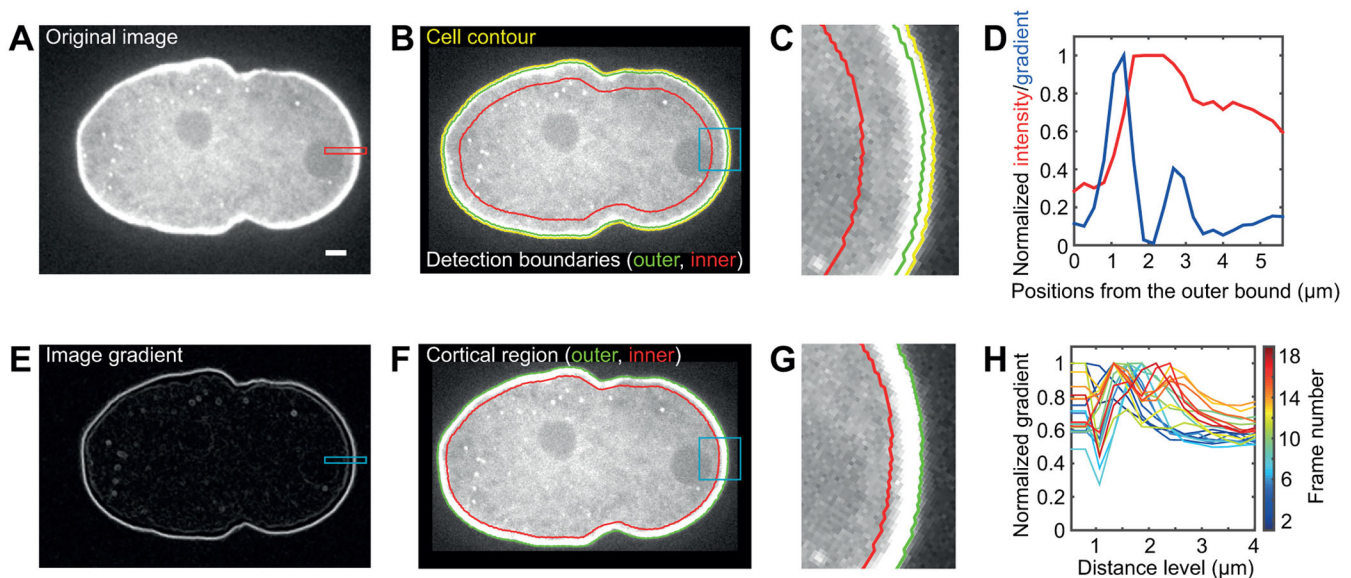


**Fig. 3. Automated extraction of a cortical region along the cell boundary.** (A) Overlay of GFP::PAR-2 and mCherry::PAR-6 images from a *C. elegans* zygote during prophase (pronuclear migration). The contrast in the image is enhanced. The red box delineates the region analyzed in D. Scale bar: 5  $\mu\text{m}$ . (B) Overlay of GFP::PAR-2 and mCherry::PAR-6 images with the detected cell contour (yellow), and initial outer and inner boundaries (green and red, respectively). (C) Magnified view of the cyan-boxed region in B. (D) Normalized profiles of image intensity (red) and intensity gradient (blue) along the outer–inner axes of boxed regions in A and E, respectively. (E) Map showing the intensity gradient of GFP::PAR-2 and mCherry::PAR-6. The cyan box delineates the region analyzed in D. (F) Cortical regions enclosed by outer (green) and inner (red) contours. (G) Magnified view of the cyan-boxed region in F. (H) Normalized profiles of intensity gradients of all image frames as a function of distance level.

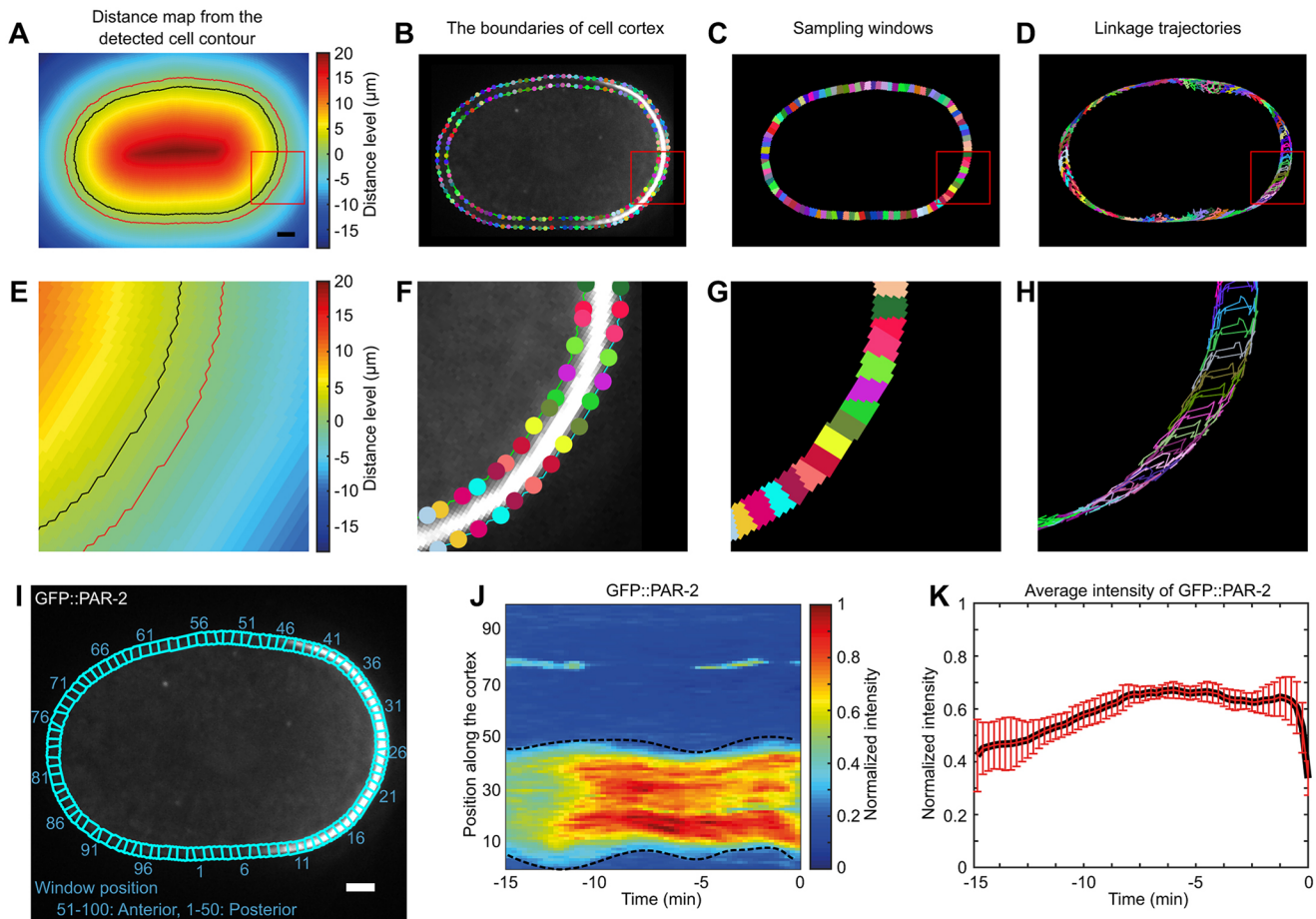


**Fig. 4. Setting and linkage of sampling windows along the cell cortex.** (A) Distance map based on the detected cell contours, overlaid with the inner (black) and outer (red) boundaries of the cortical region. The color bar indicates the distance to the cell boundary. Positive values: pixels inside the cell edge. Negative values: pixels outside the cell boundary. Scale bar: 5  $\mu$ m. (B) An overlay of the GFP::PAR-2 image with control points as shown in different colors along the inner and outer boundaries of the cell cortex. Each pair of control points is shown using the same color. (C) Sampling windows are shown along the cell cortex using different colors. (D) Linkage trajectories (as shown in different colors) of sampling windows. (E–H) Magnified views of the boxed region in A–D, respectively. (I) Representative image of a *C. elegans* zygote expressing GFP::PAR-2. Sampling windows are shown along the cell cortex. Scale bar: 5  $\mu$ m. (J) Representative kymograph of cortical intensity dynamics of GFP::PAR-2. The mean intensities of GFP::PAR-2 in each sampling window are visualized as a 2D heat map with the horizontal axis as the time frame and the vertical axis as the position of sampling windows. Black dashed lines are manually drawn to highlight boundaries between the anterior and the posterior cortical domains. The color bar shows protein intensities normalized to the maximum in the heatmap. Times stated are relative to the onset of cytokinesis in the first cell division. (K) The graphs depict average fluorescence intensity of GFP::PAR-2 within the posterior cortical domain. Data represent mean  $\pm$  s.d. from four samples.

analysis, we next evaluated the sensitivity of ImaEdge to image noise. We used the cell contours and the detected cortex from the merged images of GFP::PAR-2 and mCherry::PAR-6 channels from a *C. elegans* zygote obtained under typical experimental conditions as the ground-truth information for error measurement. We determined the signal-to-noise ratio (SNR) to be  $\sim 17$  dB from this test movie (Fig. 5A). Subsequently, we synthesized noise-added images at varying levels (SNR from 17 dB to 10 dB) by introducing Gaussian noise to the ground-truth movie (Fig. 5B; Fig. S2). We then assessed the accuracy of cell edge segmentation during the adaptive radial thresholding. Although strong noise intensity can be clearly observed in low-SNR images, the overlay of identified cell contours from synthesized noisy images did not show large deviations from the original cell contours. The errors, calculated as the piecewise minimum distances between segmented and ground-truth contour pixels along the ground-truth cell contour (Fig. 5C,D), were generally within 1  $\mu$ m. The average root-mean-square (RMS) error of a segmented cell contour at a specific noise level can also be visualized as an error map (Fig. 5E). These

analyses indicate that segmentation by ImaEdge is relatively resistant to noise over a large range of noise levels (SNR from 12 dB to 17 dB).

However, we noticed small fluctuations in the very low-SNR images (SNR from 10 dB to 11 dB). This was probably due to the intrinsic inconsistency in quality over the frames of the ground-truth movies. To understand the general trend of how image noise influences our segmentation accuracy, we determined the average RMS error over all frames (Fig. 5F). As expected, the segmentation error increased with higher noise levels. However, small standard deviations for movies with SNR from 13 dB to 17 dB were observed, indicating that the inconsistencies in movie quality do have minor influences on accurate cell segmentations.

We next investigated how the quantification of protein spatiotemporal dynamics is affected by image noise. Errors were estimated using the differences in the centroid positions of the sampling windows under various noise levels. This metric therefore takes into account both the errors in the cell segmentation and cortex

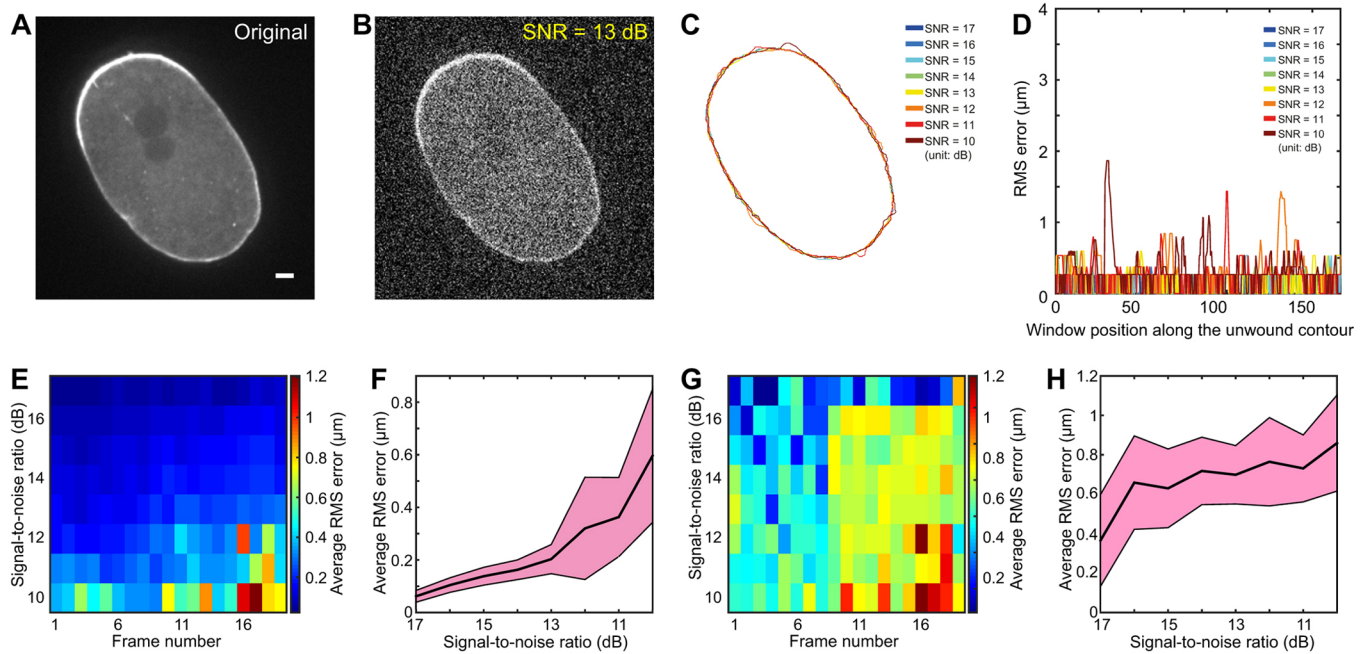


**Fig. 5. Sensitivity analysis of ImaEdge.** (A–D) Sensitivity analysis based on a single image frame from a *C. elegans* zygote. (A) Representative image of two merged channels (GFP::PAR-2 and mCherry::PAR-6) as the ground-truth data set. Scale bar: 5  $\mu$ m. (B) Image with introduced noise, representing an SNR of 13 dB. (C) An overlay of the detected cell contours from images with varying levels of introduced noise (SNR=10–17). (D) A graph showing RMS errors of the detected cell contours from images varying levels of introduced noise (SNR=10–17), as a function of distance along the unwound contour of the ground-truth data set. (E,F) Sensitivity analysis for cell contour detection. (E) A RMS error map calculated as a function of image noise (SNR) versus image frame number. (F) Average RMS error (black line) of cell contour detection as a function of image noise (SNR) from a time-lapse movie. Pink area depicts s.d. (G,H) Sensitivity analysis for cell cortex detection. (G) A RMS error map calculated as a function of image noise (SNR) versus image frame number. (H) Average RMS error (black line) of cell cortex detection as a function of image noise (SNR) in a time-lapse movie. Pink area depicts s.d.

detection steps. As expected, the decrease in SNR translates to an increase in sampling error, with larger variations over all noise levels compared with the previous analysis of segmentation sensitivity (Fig. 5G,H). Nevertheless, the overall RMS error of cortex sampling remained at a low level, typically within 1  $\mu$ m. Taken together, our sensitivity analysis highlights the robustness of ImaEdge in processing and analyzing movies of developing *C. elegans* zygotes over a wide range of noise levels.

### Robust cortical segmentation and measurement of cortical proteins in *C. elegans* zygotes

We applied ImaEdge to analyze the dynamics of mCherry::PAR-6 and GFP::PAR-2 at the cortex of *C. elegans* zygotes (Fig. 6A–C). The contours of the cell edge were determined from images that overlaid both GFP and mCherry channels. The defined cortical region was divided into 100 sampling windows along the entire cortex (Fig. 6A–C). Consistent with previous observations (Cuenca et al., 2003; Goehring et al., 2011), the 2D heat map depicts mutual exclusivity of mCherry::PAR-6 and GFP::PAR-2 throughout the first mitotic division (Fig. 6A–C). At the first ‘establishment’ phase after symmetry breaking, mCherry::PAR-6 was excluded from the posterior polar cortex, allowing GFP::PAR-2 to be loaded onto it. The size of the mCherry::PAR-6 and GFP::PAR-2 cortical domains gradually regressed and expanded, respectively. ImaEdge consistently captured the progressive increase in GFP::PAR-2 intensity within the posterior cortical domain until the initial over-expansion of the growing cortical GFP::PAR-2 domain was stalled and then retracted (Fig. 6A–C). In contrast, cortical intensity of mCherry::PAR-6 was generally constant during the establishment phase (Fig. 6A–C). During the following ‘maintenance’ phase, the

size of the two cortical domains reached steady state (Fig. 6A–C). These analyses demonstrated that ImaEdge is not only capable of tracing the cortex, but is also able to integrate the spatiotemporal dynamics of cortical polarity proteins during polarization.

We further assessed the capability of ImaEdge in monitoring the dynamics of mCherry::PAR-6 and GFP::PAR-2 in zygotes defective in cell polarization (Fig. 6D–I). SPD-5 is a scaffold of the pericentriolar material (PCM) and is essential for centrosome maturation during establishment phase in zygotes (Hamill et al., 2002; Woodruff et al., 2015). Depletion of SPD-5 by RNA-mediated interference (RNAi) caused loss or significant delay in segregation of cortical PAR proteins (Cowan and Hyman, 2004; Hamill et al., 2002). Analysis by ImaEdge with default parameters optimized for wild-type zygotes reflected significant delay in the exclusion of mCherry::PAR-6 and loading of GFP::PAR-2 at the posterior cortex (Fig. 6D–F). The expansion of the posterior domain in the *spd-5(RNAi)* zygote was slower than that in the control, resulting in a smaller size of the posterior domain at the steady state (Fig. 6D–F). CDC-42 is a Rho-type small GTPase that controls the complex of PAR-6 and PKC-3 during cell polarization in zygotes (Gotta et al., 2001; Kay and Hunter, 2001). CDC-42 is required to maintain PAR-6 at the anterior domain during the maintenance phase (Aceto et al., 2006; Motegi and Sugimoto, 2006) and is essential to exclude PAR-2 from the cortex (Rodriguez et al., 2017; Schonegg and Hyman, 2006). Analysis of *cdc-42(RNAi)* zygotes by ImaEdge revealed uniform cortical distribution of GFP::PAR-2 during the establishment phase, while mCherry::PAR-6 was progressively segregated into the anterior cortical domain (Fig. 6G–I). Four out of five *cdc-42(RNAi)* embryos eventually excluded GFP::PAR-2 from the anterior cortical domain where

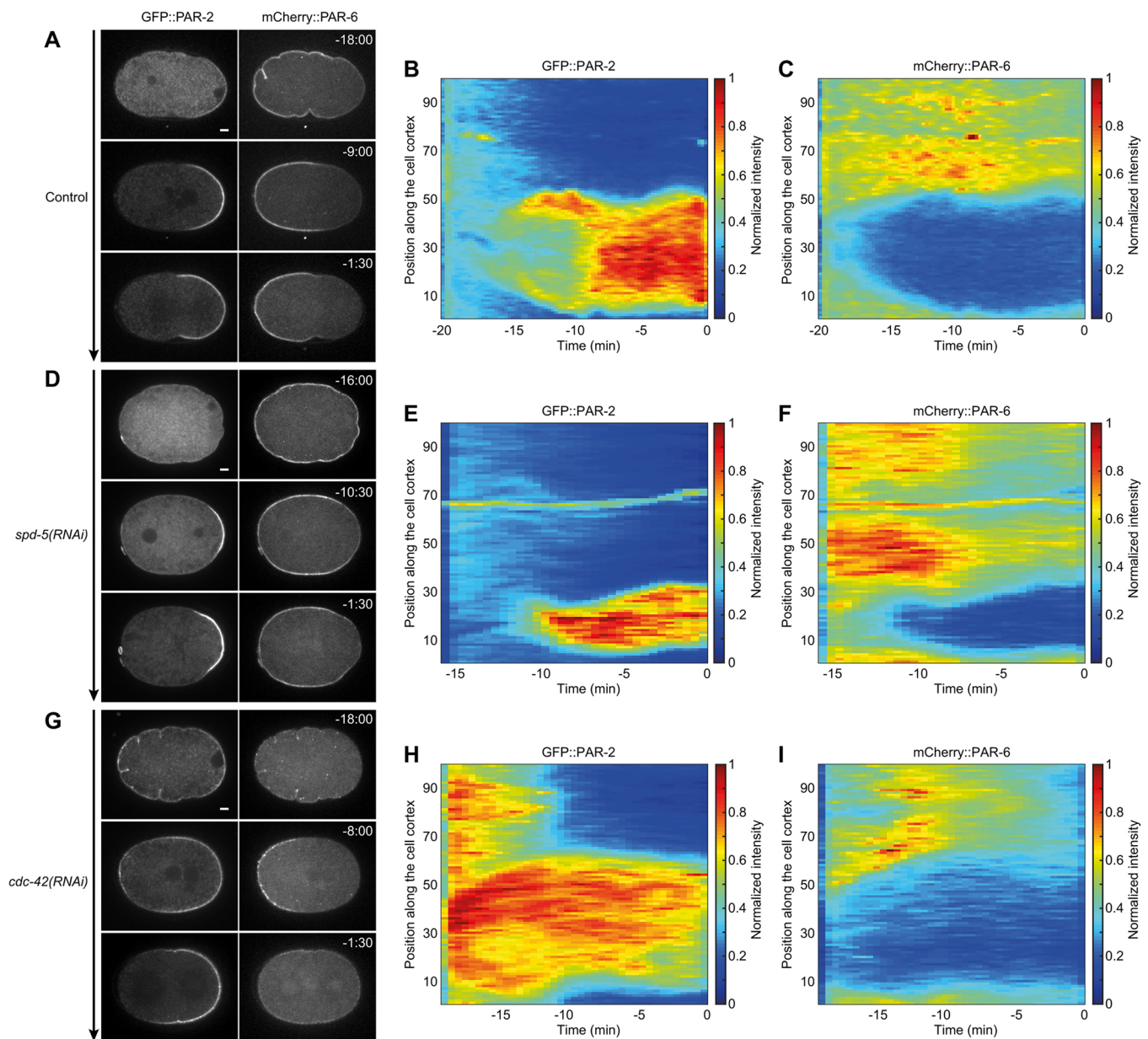


**Fig. 6. Spatio-temporal dynamics of cortical PAR proteins in *C. elegans* zygotes.** (A,D,G) Representative images of *C. elegans* zygotes co-expressing GFP::PAR-2 and mCherry::PAR-6 in control (A), *spd-5(RNAi)* (D) and *cdc-42(RNAi)* conditions (G). Scale bar: 5  $\mu$ m. (B,E,H) Representative kymographs of cortical intensity dynamics of GFP::PAR-2 in control (B), *spd-5(RNAi)* (E) and *cdc-42(RNAi)* zygotes (H). (C,F,I) Representative kymographs of cortical intensity dynamics of mCherry::PAR-6 in control (C), *spd-5(RNAi)* (F) and *cdc-42(RNAi)* zygotes (I). The mean intensities of GFP::PAR-2 and mCherry::PAR-6 in each cortical sampling window were visualized as a 2D heat map with the horizontal axis as the time frame and the vertical axis as the position of sampling windows. Color bars show protein intensities normalized to the maximum in each heatmap. Times stated are relative to the onset of cytokinesis in the first cell division. All images are representative of five zygotes from three independent experiments.

mCherry::PAR-6 became enriched (Fig. 6G–I). Thereafter, mCherry::PAR-6 disappeared from the cortex during the maintenance phase (Fig. 6G–I). Failure in cortical exclusion of PAR-2 during the establishment phase supports a model in which CDC-42 is essential to activate PKC-3 in the anterior cortical domain (Rodriguez et al., 2017). Cortical exclusion of PAR-2 from the anterior cortex during the transition from establishment to maintenance phases suggests the presence of CDC-42-independent mechanism(s) for activation of PKC-3 at the cortex. Based on these observations, ImaEdge is suitable for the spatiotemporal analysis of cortical polarity proteins, not only in wild-type zygotes but also in a

wide variety of zygotes that are defective in the process of cell polarization.

#### Sensitivity to fluorescence levels, discontinuous cortical signals and excessive shape changes in *C. elegans* zygotes

To test the sensitivity of ImaEdge under different experimental conditions, we analyzed various levels of GFP::PAR-2 in zygotes (Fig. 7A–G and Movies 4–6). The levels of *gfp::par-2* transgene expression were modified via the codon-usage optimization method (Redemann et al., 2011). Synthetic transgenes with a higher usage of adapted codons results in faster translation in the germline, thus

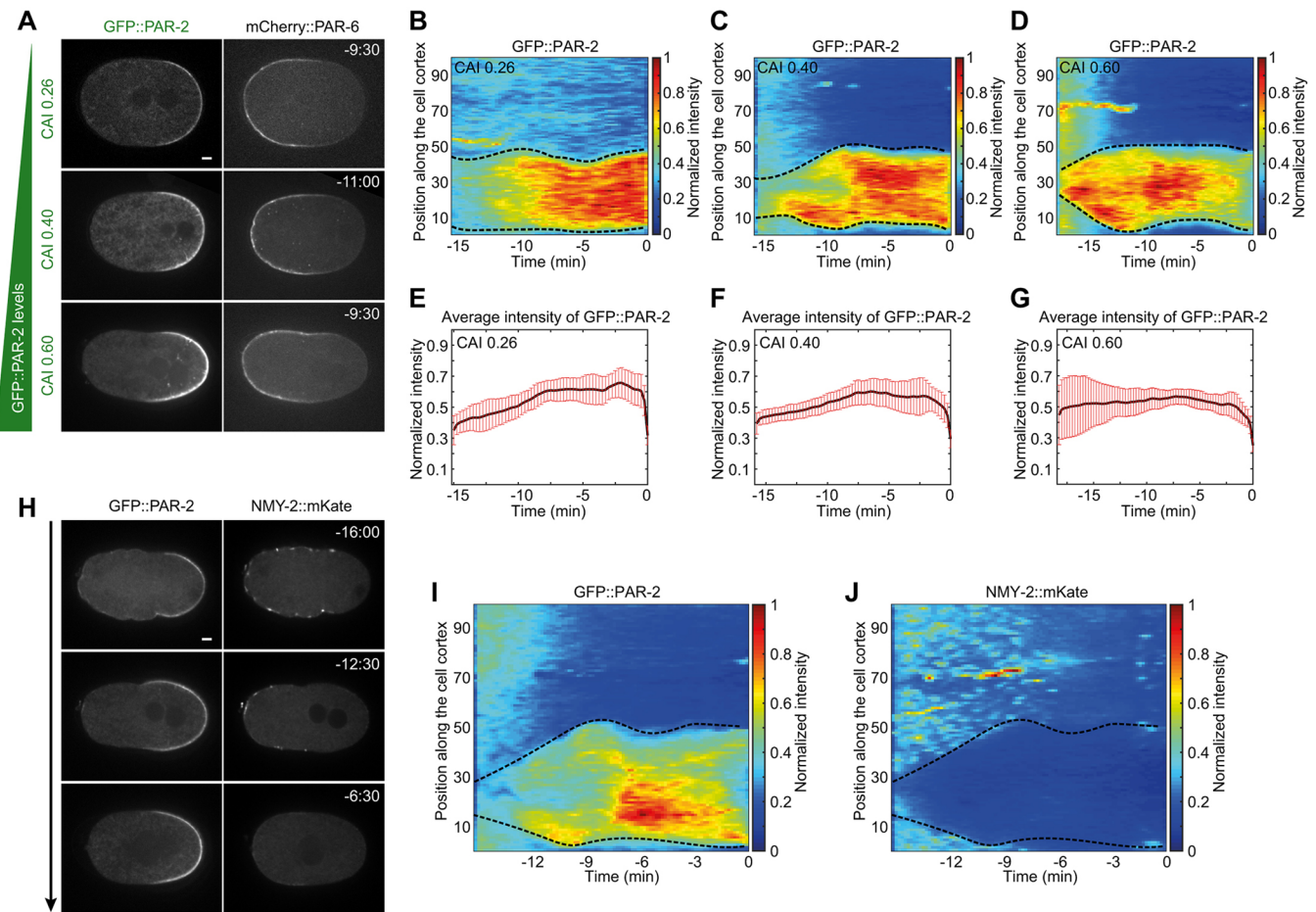


**Fig. 7. Analysis of various levels of PAR-2 and discontinuous cortical signals of NMY-2 in *C. elegans* zygotes.** (A) Representative time-lapse images of *C. elegans* zygotes expressing mCherry::PAR-6 and various levels of GFP::PAR-2 transgene. GFP::PAR-2 expression levels were optimized to varying degrees by the differential codon usage optimization method. CAI, codon adaptation index. (B–D) Representative kymographs of GFP::PAR-2 cortical intensity dynamics in zygotes expressing synthetic *gfp::par-2* transgene with CAI values of 0.26 (B), 0.40 (C) and 0.60 (D). The mean intensities of GFP::PAR-2 in each cortical sampling window were visualized as a 2D heat map with the horizontal axis as the time frame and the vertical axis as the position of sampling windows. (E–G) Average intensity of GFP::PAR-2 within the posterior cortical domains in zygotes expressing *gfp::par-2* with CAI values of 0.26 (E), 0.40 (F) and 0.60 (G). Data represent mean values  $\pm$  s.d. from five samples for each condition. (H) Representative time-lapse images of a *C. elegans* zygote expressing NMY-2::mKate and GFP::PAR-2. (I, J) Representative kymographs of cortical intensity dynamics of GFP::PAR-2 (I) and NMY-2::mKate (J). The mean intensities of NMY-2::mKate and GFP::PAR-2 in each cortical sampling window were visualized as a 2D heat map with the horizontal axis as the time frame and the vertical axis as the position of sampling windows. (B, C, D, I, J) Black dashed lines were manually drawn to reflect boundaries between the anterior and the posterior cortical domains. Color bars show protein intensities normalized to the maximum in each heatmap. All images are representative of five zygotes from three independent experiments. Times stated in A and H (min:s) are relative to the onset of cytokinesis in the first cell division. Scale bars: 5  $\mu$ m.

increasing the level of GFP::PAR-2 protein in early embryos. We imaged zygotes from transgenic animals expressing three synthetic *gfp::par-2* transgenes with codon adaptation index (CAI) values of 0.6, 0.4 and 0.26 (Fig. 7A). ImaEdge was able to define the cell edge contour and to extract the spatiotemporal dynamics of cortical GFP::PAR-2 even using the images from embryos expressing lower levels of GFP::PAR-2 (Fig. 7A–G). Consistent with a previous report (Goehring et al., 2011), the boundary between the anterior and the posterior domain was shifted toward the anterior pole in zygotes expressing higher levels of GFP::PAR-2, while conversely, the boundary was shifted toward the posterior pole in zygotes expressing lower levels of GFP::PAR-2 (Fig. 7A–D). Analysis by ImaEdge revealed that the lower levels of GFP::PAR-2 significantly retarded the expansion of the posterior cortical domain, while the higher level of GFP::PAR-2 caused efficient expansion of the posterior cortical domain (Fig. 7A–D). An increase in the level of

GFP::PAR-2 changed the kinetics of cortical loading of GFP::PAR-2 within the posterior cortex (Fig. 7B–G) and blocked the stalling-and-retraction behavior of the posterior cortical domain (Fig. 7B–D). These observations and analyses by ImaEdge support a model in which PAR-2 stimulates the expansion of the posterior cortical domain.

We next assessed the capability of ImaEdge in quantifying discontinuous signals of cortical non-muscle myosin-II heavy chain (NMY-2; Fig. 7H–J and Movie 7). Cortical NMY-2 appears as numerous foci, which undergo dynamic turnover and move toward the anterior cortex during polarity establishment (Munro et al., 2004) (Fig. 7H). Despite the discontinuous intensity of cortical NMY-2::mKate, ImaEdge achieved robust segmentation of the cell edge contour just by using the images from the NMY-2::mKate channel (Fig. 7H–J). The analysis of cortical NMY-2::mKate revealed that NMY-2 foci dynamically appeared and disappeared

during the establishment and the maintenance phases, respectively (Fig. 7J). The timing of the disappearance of NMY-2::mKate occurred simultaneously with the retraction of the posterior GFP::PAR-2 domain (Fig. 7I,J). These analyses demonstrated that ImaEdge can be effectively and reliably applied to the analysis of a wide variety of cortical proteins in polarizing zygotes.

We further tested the ability of ImaEdge to analyze the cortex in zygotes that exhibit excessive cell shape changes. Depletion of the RhoGAP RGA-3 causes hyper-contraction of cortical actomyosin because of a failure in the inactivation of the small GTPase RHO-1 (Schmutz et al., 2007; Schonegg et al., 2007). Although ImaEdge was able to consistently track both cortical PAR-6::GFP and cortical NMY-2::mKate in zygotes showing excessive ruffling, it was unable to recognize the deeper cortical invaginations, where cortical PAR-6 and NMY-2::mKate signals penetrated into the cytoplasm (Fig. S3). Similarly, ImaEdge was not able to recognize cortical signals at cleavage furrows and subsequent cell–cell contact sites (see Fig. 8).

### Monitoring polarization of PAR proteins in *C. elegans* two-cell embryos

We next applied ImaEdge to analyze the polarization of PAR proteins during the second cell division by extracting cortical information along the surface of two-cell stage embryos. In two-cell stage embryos, the anterior cell (AB) is destined to divide symmetrically, resulting in equal inheritance of PAR proteins by two daughter cells, ABa and ABp (Fig. 8A and Movie 8). In contrast, the posterior cell (P1) is engaged to undergo asymmetric cell division, resulting in asymmetric inheritance of PAR-6 and PAR-2 by two daughter cells, EMS and P2, respectively (Fig. 8A). Analysis by ImaEdge was able to automatically detect dynamic processes in the segregation of mCherry::PAR-6 to the anterovertical cortex, and that of GFP::PAR-2 to the posterior polar cortex in P1 cells (Fig. 8B–E). In contrast to zygotes, P1 cells initially showed GFP::PAR-2 localizing throughout the cortex (Fig. 8A,B). During prophase, GFP::PAR-2 was excluded from the anterovertical cortex, where mCherry::PAR-6 became enriched (Fig. 8A–C). The size and intensity of the posteriorly localized cortical GFP::PAR-2 domain was stable until prometaphase, when it started to polarize towards one side of the lateral cortex (Fig. 8B,D). Subsequently, the GFP::PAR-2 domain was inherited by the posterior-positioned daughter cell, P2.

We next tested whether ImaEdge was sensitive enough to detect the abnormal behavior of GFP::PAR-2 in P1 cells. We performed an RNAi-based screen to look for genes that, when depleted, do not affect PAR-2 polarization in zygotes, but whose absence would compromise PAR-2 behavior in P1 cells. Among the candidates tested, we found that the depletion of *zyg-1* fulfilled the above requirements. ZYG-1 is a member of the *Polo*-like kinase 4 family and is essential for centriole replication. P1 cells depleted of ZYG-1 failed to divide, because of the absence of bipolar spindles during the second cell division. Zygotes treated with *zyg-1* (RNAi) exhibited cortical PAR domains with normal intensities and size during the first cell division (Fig. 8F and Movie 9). Analysis by ImaEdge showed that the distribution of GFP::PAR-2 at the posterior cortex was maintained in the P1 cell until prometaphase, when it started to disappear from the posterior cortex or remained localized throughout the entire P1 cell cortex (Fig. 8G–J). Given that P1 cells polarize in a cell-autonomous manner (independent of the anterior cell, AB) (Priess and Thomson, 1987), these observations suggest that the formation of a bipolar mitotic spindle is essential for the establishment of a polarized PAR-2 domain in P1 cells. These

analyses demonstrated the versatility of ImaEdge in quantifying cortical dynamics of polarity proteins not only at the one-cell stage, but also in multicellular-stage embryos.

### DISCUSSION

In this study, we have introduced an image analysis platform, ImaEdge, which allows for efficient quantitative analysis of cortical proteins in living embryos. ImaEdge enables the automatic detection of cell edge contours and accurate extraction of the cell cortex from time-lapse movies. Profiles depicting the fluorescence intensities of cortical proteins can be sampled using a finite number of boxes, allowing the spatiotemporal dynamics of cortical proteins to be represented as 2D heat maps. As pioneered earlier (Machacek et al., 2009), the heat map of cortical protein signals can also be averaged for statistical analysis. The radial adaptive segmentation method we propose here is capable of robust extraction of the entire cell cortex, even those with inhomogeneous distribution of cortical proteins in *C. elegans* embryos. ImaEdge comes with a set of default parameters for automatic segmentation of the cortex that can analyze both wild-type and polarity-defective mutant embryos. The current version of ImaEdge is unable to handle multiple cells. However, this step can be tackled in a relatively straightforward way by detecting multiple ROIs and analyzing them separately. In the meantime, although ImaEdge currently fails to differentiate between cells in multicellular embryos, it is still able to extract the cortical information along the surface of the embryos.

As described in Table S3, users may choose to adjust any parameters to suit their systems of interest, such as the number of sector sub-regions, the size of median filter, the number of the sampling windows and whether to use radial adaptive segmentation or simple segmentation (faster for simple datasets). In terms of the ease of further development, ImaEdge adopts simple algorithms that can be readily understood and modified by researchers in the fields of cell biology and developmental biology. Image segmentation of both the cell boundary and the cortex by ImaEdge requires only rough ranges of a couple of parameters (Table S3), because the program can scan these parameters and define the most suitable parameter values for each frame in time-lapse movies. Although the optimal parameters may be variable for different frames, the same parameter scopes can be generally used to process all frames.

ImaEdge is currently optimized for time-series images of *C. elegans* embryos, whose motility and cell volume changes are generally negligible (except during cytokinesis). Therefore, the constant radial sub-division mask can be determined from the first frame and then applied for all frames. Our method of adaptive radial segmentation can be readily extended to cases involving cell migration and extensive cell shape/volume changes by invoking a radially partitioned mask adaptively constructed for the cell image of each frame. Based on the extracted contours and their corresponding distance maps, protein quantities at the cortex can be sampled in a similar fashion and aligned to multiple references, such as center of mass, nuclear position or protruding cell edges.

The segmentation process used by ImaEdge is dependent on the local contrast between the cell and the background, as calculated using Otsu's method. Thus, there are currently two limitations in detection of the highly-convoluted cortex and the multicellular case where the cortex from neighboring cells are in close apposition. Ultimately, these limitations stem from the resolution limit of the imaging system. In the first case, regions of the highly convoluted cortex with high radius of curvature are not well resolved, and thus these errors inevitably propagate into any subsequent processing. In the second case, the difficulty stems from resolving one cortex from

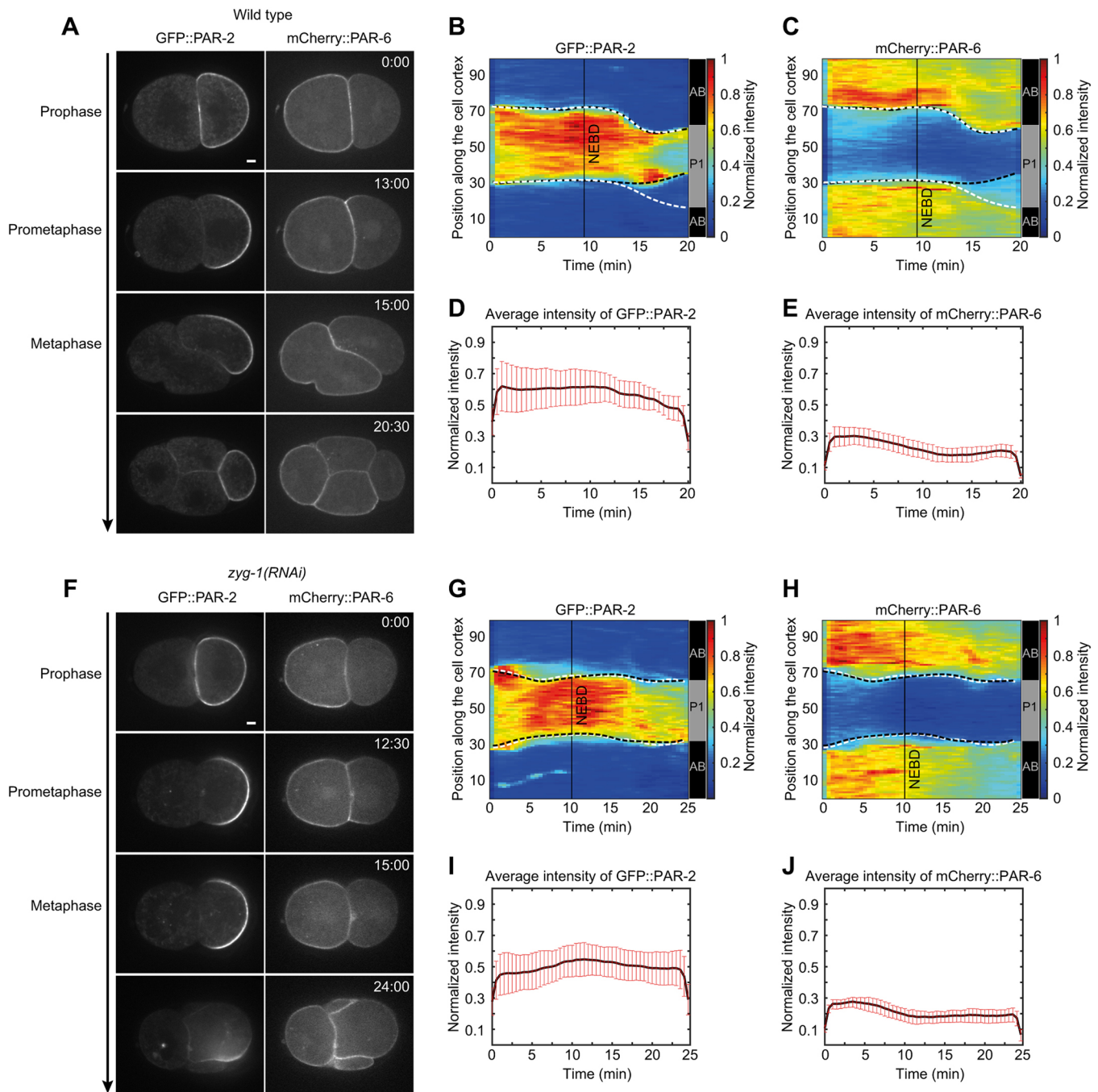


**Fig. 8. Monitoring polarization of PAR proteins in two-cell-stage *C. elegans* embryos.** (A) Representative time-lapse images of a two-cell-stage embryo co-expressing mCherry::PAR-6 and GFP::PAR-2. (B,C) Representative kymographs of cortical intensity dynamics of GFP::PAR-2 (B) and mCherry::PAR-6 (C) in a two-cell stage embryo. The mean intensities of GFP::PAR-2 in each cortical sampling window were visualized as a 2D heat map with the horizontal axis as the time frame and the vertical axis as the position of sampling windows. (D,E) Average fluorescence intensity of GFP::PAR-2 (D) and mCherry::PAR-6 (E) at the posterior cortical domains in wild-type embryos. Data represent mean values  $\pm$  s.d. from five samples. (F) Representative time-lapse images of a two-cell-stage *zyg-1(RNAi)* embryo co-expressing mCherry::PAR-6 and GFP::PAR-2. (G,H) Representative kymographs of cortical intensity dynamics of GFP::PAR-2 (G) and mCherry::PAR-6 (H) in a two-cell-stage *zyg-1(RNAi)* embryo. The mean intensities of GFP::PAR-2 in each cortical sampling window were visualized as a 2D heat map with the horizontal axis as the time frame and the vertical axis as the position of sampling windows. (I,J) Average fluorescence intensity of GFP::PAR-2 (I) and mCherry::PAR-6 (J) at the posterior cortical domains in *zyg-1(RNAi)* embryos. Data represent mean  $\pm$  s.d. from five samples. In B,C, G,H, black dashed lines were manually drawn to highlight PAR-2 localization in the embryo. White dashed lines were manually drawn to reflect boundaries between AB and P1 cells. Black lines indicate the timing of nuclear envelope break down (NEBD), which occurs during prometaphase. Color bars show protein intensities normalized to the maximum in each heatmap. All images are representative of five zygotes from three independent experiments. The times stated in A and F (min:s) are relative to the end of cytokinesis in the first cell division. Scale bars: 5  $\mu$ m.

another, since the cell-to-cell gap is well below the diffraction limit. These limitations are clearly demonstrated in examples from Fig. 8 whereby ImaEdge can reveal the distinct behaviors of PAR proteins

in two-cell-stage embryos between wild-type and *zyg-1(RNAi)* conditions, but is unable to recognize their distribution at the contact between AB and P1 blastomeres. Similarly, ImaEdge performs well

on wild-type embryos, but is unable to detect the deeper cortical invaginations in hyper-contractile *rga-3(RNAi)* embryos. Possible solutions to these problems may require super-resolution microscopy approaches (Bertocchi et al., 2013). With current diffraction-limited microscopy, we therefore recommend users to carefully examine cortical regions defined by ImaEdge, when deeper cortical invaginations and furrows are prominent in the target cell(s).

The current version of ImaEdge is designed to analyze two-dimensional time-series images. It might be possible to extend an analogous approach to analyze higher-dimensional datasets, such as 4D images (three-dimensional time-series images). The 3D ROI can be radially divided into a finite number of cone-shaped sub-regions for adaptive segmentation. The 3D cell cortex determined using a 3D image gradient can then be sampled by connecting a set of equally spaced control points at the segmented cell surface to their closest points at the inner surface of cell cortex. These will inevitably entail additional complexity both in terms of the algorithms and visual display of the analysis results. However, at present a more acute challenge lies in the acquisition of such datasets with sufficient duration and spatiotemporal resolution while preserving sample viability. Light-sheet microscopy may address this need but this is not yet widely available (Chen et al., 2014).

ImaEdge is fully open-source and equipped with a user-friendly graphical interface, thereby providing a ready-made platform for the cell and developmental biology community to view, modify and customize their analysis as desired [ImaEdge source code and user manual can be found on GitHub (<http://github.com/KanchanawongLab>)]. For example, ImaEdge can be integrated with existing analyses, such as cell-marking methods (Murray et al., 2006; Ooi et al., 2006), imaging of cell-lineage tracing (Bao et al., 2006) or other analytical software (Boyle et al., 2006; Du et al., 2014; Santella et al., 2010, 2014). This will allow for the integrated and rigorous quantification of cortical protein dynamics in specific target cells over longer periods of embryogenesis such as those observed through *in toto* imaging (Keller et al., 2008; McMahon et al., 2008; Udan et al., 2014). We anticipate that ImaEdge will be instrumental in bringing about a deep quantitative understanding of the dynamic process of cell polarization, not only in *C. elegans* embryos, but also in a wide variety of polarized cells. ImaEdge thus provides a tool to link quantitative molecular information at the cortex to theoretical models, which marks a significant step forward for quantitative and predictive interpretation of cell polarization.

## MATERIALS AND METHODS

### Worm strains and live imaging

The *C. elegans* strains used in this study are MOT119: *unc-119(ed3) III; dds238[gfp::par-2 re-coded, CAI=0.26]; par-2(ok1723); temIs17 [mCherry::par-6]*, MOT121: *unc-119(ed3) III; temIs7[gfp::par-2 no codon optimization, CAI=0.26]; par-2(ok1723); temIs17[mCherry::par-6]*, MOT118: *unc-119(ed3) III; par-2(ok1723); dds25[gfp::par-2 re-coded, CAI, 0.41]; temIs17[mCherry::par-6]*, MOT120: *unc-119(ed3) III; dds239[gfp::par-2 re-coded, CAI=0.60]; par-2(ok1723); temIs17 [mCherry::par-6]*, MOT295: *nmy-2(cp52[nmy-2::mkate]) I; unc-119 (ed3) III; pkc-3(it309[pkc3::gfp])*. All strains were maintained at 25°C according to standard procedures (Brenner, 1974). RNAi experiments were performed by the feeding method. In short, L4440-based RNAi clones were transformed into *E. coli* HT115 cells and the transformants were inoculated into liquid LB with 500 µg/ml carbenicillin and grown at 37°C. Then, 100 µl of successfully transformed *E. coli* liquid culture was seeded onto nematode growth medium plates with 1 mM IPTG. The bacterial lawn was allowed to

grow overnight at room temperature. Worms at the L1 stage and L4 stage were transferred to feeding plates for RNAi against *zyg-1* and other genes, respectively, and incubated at 25°C.

*C. elegans* embryos were isolated from gravid hermaphrodites into egg salt buffer, placed onto coverslips, and inverted on slides with 20 µm monodisperse polystyrene beads (Bangs Labs) as a spacer. All embryos in this imaging condition completed their first mitotic cell cycle and underwent successful cytokinesis. Embryos were observed at 25°C with a CFI Plan Apochromat 60× NA1.4 oil-immersion lens on a Nikon Ti-E motorized upright microscope outfitted with a CSU-X1 spinning-disc confocal system (Yokogawa Electric) with LaserStack 491 and 561 solid-state diode lasers (Intelligent Imaging Innovation). Images with pixel size of 266.7 nm were acquired with a Photometrics Evolve512 camera (Photometrics) controlled by Metamorph (Intelligent Imaging Innovation) every 2 s using 250 ms exposure for GFP fusions and 250 ms for mKate and mCherry fusions at 20% power on the 491 and 561 lasers and 1×1 binning in the camera.

### Image analysis

In all our analysis, we used a combined image of multi-channel images (MATLAB command: *rgb2gray*) and divided the ROI into 10 sectors for radial adaptive segmentation. The intensity gradient map was computed by applying a Sobel–Feldman filter (Eqns 1–3) to the contrast-enhanced image:

$$G_x = \begin{bmatrix} +1 & 0 & -1 \\ +2 & 0 & -2 \\ +1 & 0 & -1 \end{bmatrix} * A, \quad (1)$$

$$G_y = \begin{bmatrix} +1 & +2 & +1 \\ 0 & 0 & 0 \\ -1 & -2 & -1 \end{bmatrix} * A, \quad (2)$$

$$G = \sqrt{G_x^2 + G_y^2}. \quad (3)$$

The averaged image gradient with a specific contour was then calculated according to Eqn 4:

$$G_{average} = \frac{\sum_{i=1}^n G_{x_i, y_i}}{n}, \quad (4)$$

where *A* is the original image, *G<sub>x</sub>* and *G<sub>y</sub>* are gradient maps along the *x*- and *y*-axis, *G* refers to the map of the magnitude of image gradient, and *G<sub>average</sub>* is the mean gradient along a contour containing *n* pixels. For the segmentation of cell contour and cortex, we adopt the automation function with multicore computing provided by ImaEdge. To smoothen the final heat map for each channel, we applied a Gaussian filter with standard deviations of 5 pixels (or 5 frames) along the *x*-axis and 1 pixel (or 1 sampling window) along the *y*-axis, to the original heatmap.

ImaEdge was coded in MATLAB (Release R2015a). All computations were performed on a Windows 7 workstation [Intel(R) Xeon(R) CPU E5-2640 v3 @ 2.60 GHz; RAM 192GB; 64-bit OS].

### Acknowledgements

We thank Ken Kemphues (Cornell University), Bob Goldstein and Dan Dickinson (University of North Carolina), Nathan Goehring (The Francis Crick Institute) and the *Caenorhabditis* Genetic Center for sharing *C. elegans* strains, and core facilities in the MBI and TLL for their assistance.

### Competing interests

The authors declare no competing or financial interests.

### Funding

We acknowledge funding support from the National Research Foundation Singapore (NRF) under the NRF Fellowship scheme to F.M. (NRF\_NRFF2012-08) and P.K. (NRF-NRFF-2011-04), the NRF Competitive Research Programme to P.K. (NRF2012NRF-CRP-001-084), and the Ministry of Education - Singapore Academic Research Fund Tier 2 to P.K. (MOE-T2-1-124). F.M. was also supported by the Strategic Japan-Singapore Cooperative Research Program by the Japan Science and Technology Agency and the Singapore Agency for Science, Technology, and Research (1514324022). Z.Z. is supported by the MBI Graduate Scholarship.

# Data availability

The source code can be downloaded from GitHub (<http://github.com/KanchanawongLab>). The compiled standalone software packages for Windows and Mac systems are also available from the corresponding authors on reasonable request.

# Supplementary information

Supplementary information available online at <http://jcs.biologists.org/lookup/doi/10.1242/jcs.206870.supplemental>

# References

- Aceto, D., Beers, M. and Kemphues, K. J. (2006). Interaction of PAR-6 with CDC-42 is required for maintenance but not establishment of PAR asymmetry in *C. elegans*. *Dev. Biol.* **299**, 386–397.
- Balla, T. and Varnai, P. (2009). Visualization of cellular phosphoinositide pools with GFP-fused protein-domains. *Curr. Protoc. Cell Biol.* Chapter 24, Unit 24.4.
- Bao, Z., Murray, J. I., Boyle, T., Ooi, S. L., Sandel, M. J. and Waterston, R. H. (2006). Automated cell lineage tracing in *Caenorhabditis elegans*. *Proc. Natl. Acad. Sci. USA* **103**, 2707–2712.
- Barry, D. J., Durkin, C. H., Abella, J. V. and Way, M. (2015). Open source software for quantification of cell migration, protrusions, and fluorescence intensities. *J. Cell Biol.* **209**, 163–180.
- Beatty, A., Morton, D. and Kemphues, K. (2010). The *C. elegans* homolog of *Drosophila* Lethal giant larvae functions redundantly with PAR-2 to maintain polarity in the early embryo. *Development* **137**, 3995–4004.
- Bertocchi, C., Goh, W. I., Zhang, Z. and Kanchanawong, P. (2013). Nanoscale imaging by superresolution fluorescence microscopy and its emerging applications in biomedical research. *Crit. Rev. Biomed. Eng.* **41**, 281–308.
- Biro, M., Romeo, Y., Kroschwald, S., Bovellan, M., Boden, A., Tcherkezian, J., Roux, P. P., Charras, G. and Paluch, E. K. (2013). Cell cortex composition and homeostasis resolved by integrating proteomics and quantitative imaging. *Cytoskeleton* **70**, 741–754.
- Bosgraaf, L. and Van Haastert, P. J. (2010). Quimp3, an automated pseudopod-tracking algorithm. *Cell Adh. Migr.* **4**, 46–55.
- Boyd, L., Guo, S., Levitan, D., Stinchcomb, D. T. and Kemphues, K. J. (1996). PAR-2 is asymmetrically distributed and promotes association of P granules and PAR-1 with the cortex in *C. elegans* embryos. *Development* **122**, 3075–3084.
- Boyle, T. J., Bao, Z., Murray, J. I., Araya, C. L. and Waterston, R. H. (2006). AceTree: a tool for visual analysis of *Caenorhabditis elegans* embryogenesis. *BMC Bioinformatics* **7**, 275.
- Bray, D. and White, J. G. (1988). Cortical flow in animal cells. *Science* **239**, 883–888.
- Brenner, S. (1974). The genetics of *Caenorhabditis elegans*. *Genetics* **77**, 71–94.
- Chen, B.-C., Legant, W. R., Wang, K., Shao, L., Milkie, D. E., Davidson, M. W., Janetopoulos, C., Wu, X. S., Hammer, J. A., Liu, Z. III et al. (2014). Lattice light-sheet microscopy: imaging molecules to embryos at high spatiotemporal resolution. *Science* **346**, 1257998.
- Clark, A. G., Wartlick, O., Salbreux, G. and Paluch, E. K. (2014). Stresses at the cell surface during animal cell morphogenesis. *Curr. Biol.* **24**, R484–R494.
- Cowan, C. R. and Hyman, A. A. (2004). Centrosomes direct cell polarity independently of microtubule assembly in *C. elegans* embryos. *Nature* **431**, 92–96.
- Cowan, C. R. and Hyman, A. A. (2006). Cyclin E-Cdk2 temporally regulates centrosome assembly and establishment of polarity in *Caenorhabditis elegans* embryos. *Nat. Cell Biol.* **8**, 1441–1447.
- Cuenca, A. A., Schetter, A., Aceto, D., Kemphues, K. and Seydoux, G. (2003). Polarization of the *C. elegans* zygote proceeds via distinct establishment and maintenance phases. *Development* **130**, 1255–1265.
- Dimopoulos, S., Mayer, C. E., Rudolf, F. and Stelling, J. (2014). Accurate cell segmentation in microscopy images using membrane patterns. *Bioinformatics* **30**, 2644–2651.
- Dormann, D., Libotte, T., Weijer, C. J. and Bretschneider, T. (2002). Simultaneous quantification of cell motility and protein-membrane-association using active contours. *Cell Motil. Cytoskeleton* **52**, 221–230.
- Du, Z., Santella, A., He, F., Tiongson, M. and Bao, Z. (2014). De novo inference of systems-level mechanistic models of development from live-imaging-based phenotype analysis. *Cell* **156**, 359–372.
- Ersay, I., Bunyak, F., Mackey, M. A. and Palaniappan, K. (2008a). Cell segmentation using hessian-based detection and contour evolution with directional derivatives. *Proc. Int. Conf. Image Proc.* **2008**, 1804–1807.
- Ersay, I., Bunyak, F., Palaniappan, K., Sun, M. and Forgacs, G. (2008b). Cell spreading analysis with directed edge profile-guided level set active contours. *Med. Image Comput. Comput. Assist. Interv.* **11**, 376–383.
- Etemad-Moghadam, B., Guo, S. and Kemphues, K. J. (1995). Asymmetrically distributed PAR-3 protein contributes to cell polarity and spindle alignment in early *C. elegans* embryos. *Cell* **83**, 743–752.
- Goehring, N. W., Trong, P. K., Bois, J. S., Chowdhury, D., Nicola, E. M., Hyman, A. A. and Grill, S. W. (2011). Polarization of PAR proteins by advective triggering of a pattern-forming system. *Science* **334**, 1137–1141.
- Goldstein, B. and Macara, I. G. (2007). The PAR proteins: fundamental players in animal cell polarization. *Dev. Cell* **13**, 609–622.
- Gotta, M., Abraham, M. C. and Ahringer, J. (2001). CDC-42 controls early cell polarity and spindle orientation in *C. elegans*. *Curr. Biol.* **11**, 482–488.
- Guo, S. and Kemphues, K. J. (1995). par-1, a gene required for establishing polarity in *C. elegans* embryos, encodes a putative Ser/Thr kinase that is asymmetrically distributed. *Cell* **81**, 611–620.
- Hamill, D. R., Severson, A. F., Carter, J. C. and Bowerman, B. (2002). Centrosome maturation and mitotic spindle assembly in *C. elegans* require SPD-5, a protein with multiple coiled-coil domains. *Dev. Cell* **3**, 673–684.
- Hao, Y., Boyd, L. and Seydoux, G. (2006). Stabilization of cell polarity by the *C. elegans* RING protein PAR-2. *Dev. Cell* **10**, 199–208.
- Held, M., Schmitz, M. H. A., Fischer, B., Walter, T., Neumann, B., Olma, M. H., Peter, M., Ellenberg, J. and Gerlich, D. W. (2010). CellCognition: time-resolved phenotype annotation in high-throughput live cell imaging. *Nat. Methods* **7**, 747–754.
- Hodneland, E., Kögel, T., Frei, D. M., Gerdes, H.-H. and Lundervold, A. (2013). CellSegm – a MATLAB toolbox for high-throughput 3D cell segmentation. *Source Code Biol. Med.* **8**, 16.
- Hooge, C., Constantinescu, A.-T., Schwager, A., Goehring, N. W., Kumar, P. and Hyman, A. A. (2010). LGL can partition the cortex of one-cell *Caenorhabditis elegans* embryos into two domains. *Curr. Biol.* **20**, 1296–1303.
- Hung, T. J. and Kemphues, K. J. (1999). PAR-6 is a conserved PDZ domain-containing protein that colocalizes with PAR-3 in *Caenorhabditis elegans* embryos. *Development* **126**, 127–135.
- Kay, A. J. and Hunter, C. P. (2001). CDC-42 regulates PAR protein localization and function to control cellular and embryonic polarity in *C. elegans*. *Curr. Biol.* **11**, 474–481.
- Keller, P. J., Schmidt, A. D., Wittbrodt, J. and Stelzer, E. H. K. (2008). Reconstruction of zebrafish early embryonic development by scanned light sheet microscopy. *Science* **322**, 1065–1069.
- Kemphues, K. (2000). PARing embryonic polarity. *Cell* **101**, 345–348.
- Knoblich, J. A. (2010). Asymmetric cell division: recent developments and their implications for tumour biology. *Nat. Rev. Mol. Cell Biol.* **11**, 849–860.
- Li, F., Zhou, X., Zhao, H. and Wong, S. T. C. (2009). Cell segmentation using front vector flow guided active contours. *Med. Image Comput. Comput. Assist. Interv.* **12**, 609–616.
- Machacek, M., Hodgson, L., Welch, C., Elliott, H., Pertz, O., Nalbant, P., Abell, A., Johnson, G. L., Hahn, K. M. and Danuser, G. (2009). Coordination of Rho GTPase activities during cell protrusion. *Nature* **461**, 99–103.
- McMahon, A., Supatto, W., Fraser, S. E. and Stathopoulos, A. (2008). Dynamic analyses of *Drosophila* gastrulation provide insights into collective cell migration. *Science* **322**, 1546–1550.
- Motegi, F. and Sugimoto, A. (2006). Sequential functioning of the ECT-2 RhoGEF, RHO-1 and CDC-42 establishes cell polarity in *Caenorhabditis elegans* embryos. *Nat. Cell Biol.* **8**, 978–985.
- Motegi, F., Zonies, S., Hao, Y., Cuenca, A. A., Griffin, E. and Seydoux, G. (2011). Microtubules induce self-organization of polarized PAR domains in *Caenorhabditis elegans* zygotes. *Nat. Cell Biol.* **13**, 1361–1367.
- Munro, E., Nance, J. and Priess, J. R. (2004). Cortical flows powered by asymmetrical contraction transport PAR proteins to establish and maintain anterior-posterior polarity in the early *C. elegans* embryo. *Dev. Cell* **7**, 413–424.
- Murray, J. I., Bao, Z., Boyle, T. J. and Waterston, R. H. (2006). The lineage of fluorescently-labeled *Caenorhabditis elegans* embryos with StarryNite and AceTree. *Nat. Protoc.* **1**, 1468–1476.
- Myers, G. (2012). Why bioimage informatics matters. *Nat. Methods* **9**, 659–660.
- Nejati Javaremi, A., Unsworth, C. P. and Graham, E. S. (2013). A cell derived active contour (CDAC) method for robust tracking in low frame rate, low contrast phase microscopy – an example: the human hNT astrocyte. *PLoS ONE* **8**, e82883.
- O’Connell, K. F., Maxwell, K. N. and White, J. G. (2000). The spd-2 gene is required for polarization of the anteroposterior axis and formation of the sperm asters in the *Caenorhabditis elegans* zygote. *Dev. Biol.* **222**, 55–70.
- Ooi, S. L., Priess, J. R. and Henikoff, S. (2006). Histone H3.3 variant dynamics in the germline of *Caenorhabditis elegans*. *PLoS Genet.* **2**, e97.
- Otsu, N. (1979). A threshold selection method from gray-level histograms. *IEEE Trans. Sys. Man. Cyber* **9**, 62–66.
- Priess, J. R. and Thomson, J. N. (1987). Cellular interactions in early *C. elegans* embryos. *Cell* **48**, 241–250.
- Redemann, S., Schloissnig, S., Ernst, S., Pozniakowsky, A., Ayloo, S., Hyman, A. A. and Bringmann, H. (2011). Codon adaptation-based control of protein expression in *C. elegans*. *Nat. Methods* **8**, 250–252.
- Rodriguez, J., Peglion, F., Martin, J., Hubatsch, L., Reich, J., Hirani, N., Gubieda, A., Roffey, J., Fernandes, A., St Johnston, D. et al. (2017). aPKC cycles between functionally distinct PAR protein assemblies to drive cell polarity. *Dev. Cell* **42**, 400–415.e9.
- Rodriguez-Boulant, E. and Macara, I. G. (2014). Organization and execution of the epithelial polarity programme. *Nat. Rev. Mol. Cell Biol.* **15**, 225–242.
- Salbreux, G., Charras, G. and Paluch, E. (2012). Actin cortex mechanics and cellular morphogenesis. *Trends Cell Biol.* **22**, 536–545.

- Santella, A., Du, Z., Nowotschin, S., Hadjantonakis, A.-K. and Bao, Z.** (2010). A hybrid blob-slice model for accurate and efficient detection of fluorescence labeled nuclei in 3D. *BMC Bioinformatics* **11**, 580.
- Santella, A., Du, Z. and Bao, Z.** (2014). A semi-local neighborhood-based framework for probabilistic cell lineage tracing. *BMC Bioinformatics* **15**, 217.
- Schmutz, C., Stevens, J. and Spang, A.** (2007). Functions of the novel RhoGAP proteins RGA-3 and RGA-4 in the germ line and in the early embryo of *C. elegans*. *Development* **134**, 3495–3505.
- Schonegg, S. and Hyman, A. A.** (2006). CDC-42 and RHO-1 coordinate actomyosin contractility and PAR protein localization during polarity establishment in *C. elegans* embryos. *Development* **133**, 3507–3516.
- Schonegg, S., Constantinescu, A. T., Hoege, C. and Hyman, A. A.** (2007). The Rho GTPase-activating proteins RGA-3 and RGA-4 are required to set the initial size of PAR domains in *Caenorhabditis elegans* one-cell embryos. *Proc. Natl. Acad. Sci. USA* **104**, 14976–14981.
- Schumacher, J. M., Ashcroft, N., Donovan, P. J. and Golden, A.** (1998). A highly conserved centrosomal kinase, AIR-1, is required for accurate cell cycle progression and segregation of developmental factors in *Caenorhabditis elegans* embryos. *Development* **125**, 4391–4402.
- Song, T. H., Sanchez, V., Eldaly, H. and Rajpoot, N.** (2017). Dual-channel active contour model for megakaryocytic cell segmentation in bone marrow trephine histology images. *IEEE Trans. Biomed. Eng.* **64**, 2913–2923.
- St Johnston, D. and Ahringer, J.** (2010). Cell polarity in eggs and epithelia: parallels and diversity. *Cell* **141**, 757–774.
- Tabuse, Y., Izumi, Y., Piano, F., Kempfues, K. J., Miwa, J. and Ohno, S.** (1998). Atypical protein kinase C cooperates with PAR-3 to establish embryonic polarity in *Caenorhabditis elegans*. *Development* **125**, 3607–3614.
- Tsygankov, D., Bilancia, C. G., Vitriol, E. A., Hahn, K. M., Peifer, M. and Elston, T. C.** (2014). CellGeo: a computational platform for the analysis of shape changes in cells with complex geometries. *J. Cell Biol.* **204**, 443–460.
- Udan, R. S., Piazza, V. G., Hsu, C. W., Hadjantonakis, A.-K. and Dickinson, M. E.** (2014). Quantitative imaging of cell dynamics in mouse embryos using light-sheet microscopy. *Development* **141**, 4406–4414.
- Wang, Q., Niemi, J., Tan, C. M., You, L. and West, M.** (2010). Image segmentation and dynamic lineage analysis in single-cell fluorescence microscopy. *Cytometry A* **77**, 101–110.
- Woodruff, J. B., Wueseke, O., Viscardi, V., Mahamid, J., Ochoa, S. D., Bunkenborg, J., Widlund, P. O., Pozniakovsky, A., Zanin, E., Bahmanyar, S. et al.** (2015). Centrosomes. Regulated assembly of a supramolecular centrosome scaffold in vitro. *Science* **348**, 808–812.
- Wu, P., Yi, J., Zhao, G., Huang, Z., Qiu, B. and Gao, D.** (2015). Active contour-based cell segmentation during freezing and its application in cryopreservation. *IEEE Trans. Biomed. Eng.* **62**, 284–295.